Journal of Aerosol Science 86 (2015) 55–68

Contents lists available at ScienceDirect

Journal of Aerosol Science

journal homepage: www.elsevier.com/locate/jaerosci

# Unsteady bipolar diffusion charging in aerosol neutralisers: A non-dimensional approach to predict charge distribution equilibrium behaviour

Jean L. de La Verpilliere [a,*], Jacob J. Swanson [b], Adam M. Boies [a]

[a] Engineering Department, University of Cambridge, Trumpington Street, CB2 1PZ Cambridge, UK
[b] Department of Integrated Engineering, Minnesota State University Mankato, Mankato, MN 56001, USA

ARTICLE INFO

*Article history:*
Received 8 October 2014
Received in revised form
14 February 2015
Accepted 30 March 2015
Available online 16 April 2015

*Keywords:*
Nanotechnology
Size distribution measurement
Neutraliser
Bipolar diffusion charging
Non-equilibrium
$n \cdot t$ product rule

ABSTRACT

High total particle concentration and small particle size are common features of aerosols encountered in the field of aerosol-based nanotechnology that can potentially lead to non-equilibrium issues in the neutraliser upon SMPS characterisation, resulting in large errors in size distribution measurements. Experiments show that the commonly assumed $n \cdot t$ product rule fails to predict equilibrium behaviour in aerosol neutralisers under these conditions, as it does not capture the influence of total particle concentration and particle size. The aim of this work is to provide an equilibrium indicator that identifies situations where equilibrium is not reached in the neutraliser as a function of residence time, ion generation rate, total particle concentration, and particle size. Bipolar diffusion charging equations are solved numerically in a one-dimensional model first, and a non-dimensional analysis of the results is carried out in order to map equilibrium behaviour as a function of two non-dimensional groups, the non-dimensional ion concentration, and the non-dimensional neutraliser residence time. Solving the three-dimensional form of the charging equations in the geometry of the neutraliser then enables one to find good agreement in terms of equilibrium behaviour between experiments and predictions from the non-dimensional model. The three-dimensional model captures the complexity of the physics of unsteady particle charging inside a neutraliser. This work then discusses this as a new approach to non-equilibrium behaviour prediction in neutralisers, providing a tool supplementing the $n \cdot t$ product rule that can be used in practice.


## 1. Introduction

Growing interest in the characterisation of the smaller diameter range ($<35$ nm) of ultrafine particles at high concentrations (up to $10^{13}$ m$^{-3}$) for purposes of combustion analysis and nanomaterial production has led to increasingly stringent demands on aerosol instrumentation (Biskos, Yurteri, & Schmidt-Ott, 2008). Under these conditions, typical methods of mobility characterisation that rely on diffusion charging prove problematic. The collision kernel between particles and ions decrease with particle diameter, where particle attachment coefficients with a typical neutraliser ion is

* Corresponding author. Tel: +44 7 912 986 000.
*E-mail address:* jld51@cam.ac.uk (J.L. de La Verpilliere).

http://dx.doi.org/10.1016/j.jaerosci.2015.03.006
0021-8502/

**Nomenclature**

| | |
|---|---|
| $\alpha$ | ion–ion recombination rate ($m^3\,s^{-1}$) |
| $\beta^{\pm}_{\pm i}$ | attachment coefficient of a $\pm$ ion with a particle of a given diameter bearing $\pm i$ net elementary charges ($m^3\,s^{-1}$) |
| $d_p$ | particle diameter (nm) |
| $f^{Unsteady}_{\pm i}$ | fraction of particles of a given diameter bearing $\pm i$ net elementary charges as computed by the charging model or measured experimentally |
| $f^{Wied}_{\pm i}$ | fraction of particles of a given diameter bearing $\pm i$ net elementary charges as predicted by Wiedensohler equilibrium interpolation |
| $J$ | equilibrium indicator: relative difference to equilibrium levels in terms of $+1$ charge fraction |
| $\hat{N}$ | non-dimensional ion concentration |
| $\hat{\tau}$ | non-dimensional neutraliser residence time |
| $n^{\pm}$ | concentration of $\pm$ polarity ions ($m^{-3}$) |
| $\overline{n_0}$ | particle-weighted ion concentration ($m^{-3}$) |
| $N_{\pm i}$ | concentration of particles of a given diameter bearing $\pm i$ net elementary charges ($m^{-3}$) |
| $N_{tot}$ | total particle concentration ($m^{-3}$) |
| $P_{Coll}$ | collision probability between the average ion entering the limiting sphere and a neutral particle of a given diameter |
| $q$ | ion generation rate ($m^{-3}\,s^{-1}$) |
| $\tau_{plug}$ | neutraliser residence time assuming plug-flow (s) |
| $\overline{\tau_{res}}$ | particle-averaged neutraliser residence time (s) |

ten times higher for neutral particles with diameters of 50 nm than particles 10 nm in diameter (Hoppel & Frick, 1986). High concentrations of particles reduce the ratio of ions to particles, thus decreasing the number of excess ions available for charging. Ion–ion recombination, which typically occurs at a rate $\alpha = 1.6 \cdot 10^{-12}\ m^3\ s^{-1}$ inside a neutraliser (Hoppel & Frick, 1990), limits neutraliser ion concentrations. The strongest commercially available neutralisers have ion concentrations of $\sim 10^{14}\ m^{-3}$, a value that is of the same order of magnitude as total particle concentration in many practical cases. As a consequence, ion availability might become a limiting factor in the diffusion charging process.

Particle mobility characterisation by differential mobility analysis (DMA) is a NIST-traceable standard for reference particle sizing (Vasiliou, 2005) and is described by an ISO standard (BS ISO 15900:2009(E), 2009). Scanning mobility particle sizers (SMPS) classify particles according to their electric mobility with a DMA and then count the classified particles with a condensation particle counter (CPC). In order to determine the initial particle size distribution from the CPC raw counts by a data inversion, it is necessary to control the charge distribution of the aerosol upstream of the DMA (Flagan, 2008). The typical method of controlling the particle charge is accomplished with a bipolar diffusion charger (also known as neutraliser), where particles are introduced into an ionisation chamber that contains ion species of both polarities. Ions may be generated by a variety of sources and the charging process differs only to the extent that the mass and mobilities of the ions are distinct (Kallinger, Steiner, & Szymanski, 2012). Most analyses of mobility-dependent particle charge fraction assume that the charge distribution reaches equilibrium, resulting from the balance of collisions with positive and negative ions. This equilibrium charge distribution was first described accurately by Fuchs (1963) and fundamental efforts directed at understanding ion–particle interactions at the nanoscale still continue (Gopalakrishnan, Meredith, Larriba-Andaluz, & Hogan, 2013; López-Yglesias & Flagan, 2013). Wiedensohler (1988) solved the equilibrium charging equations to give a convenient interpolation of charge distribution as a function of particle size for typical neutraliser ion properties, which is currently used for data inversion in most commercially available SMPS systems (Flagan, 2008). It is generally accepted that the validity of the equilibrium solutions can be determined using an approximation known as the $n \cdot t$ product, where $n$ is the concentration of ion pairs inside the neutraliser and $t$ is the aerosol residence time in the neutraliser. A steady state charge distribution is approached as the $n \cdot t$ product value increases. The ISO 15200:2009(E) standard states: "for an $n \cdot t$ product larger than about $10^{13}\ m^{-3}\ s$ the equilibrium charge distribution will be reached in most practical situations" (BS ISO 15900:2009(E), 2009). The ISO standard states $n \cdot t = -(1/\beta^{\pm})\ln(1-(N_{\pm p}/N_{tot}))$, where $\beta^{\pm}$ is an unspecified attachment coefficient $\sim 10^{-12}\ m^3\ s^{-1}$, $N_{tot}$ is the total particle concentration and $N_{\pm p}$ the concentration of particles bearing $\pm p$ net elementary charges. This expression is a simplified result derived by integrating ion and aerosol conservation equations followed an approach used by Adachi, Kousaka, and Okuyama (1984) among others. Liu and Pui (1974) coined the term $n \cdot t$ product in a paper where they developed a more complete microscopic model in a similar approach to the seminal paper by Fuchs (1963), relying on the flux of positive and negative ions colliding with the particle, that result in a different expression for the $n \cdot t$ product needed to reach equilibrium. Both approaches fail to capture the influence of total particle concentration, and the use of a fixed $n \cdot t$ value in all situations fails to capture the influence of particle size. The ISO standard acknowledges the limitation of the $n \cdot t$ product, stating that an "upper particle concentration limit exists beyond which the charge equilibrium condition will not be reached", but does not provide a method for determining the concentration limit. As methods for robust measurement at small particle diameters and high concentrations are sought, there is an increased need for an equilibrium charge indicator that accounts for particle size and concentration.

This work therefore aims to understand the complex influence of ion concentration, neutraliser residence time, total particle concentration, and particle size on the non-equilibrium behaviour of aerosol bipolar diffusion charging inside a

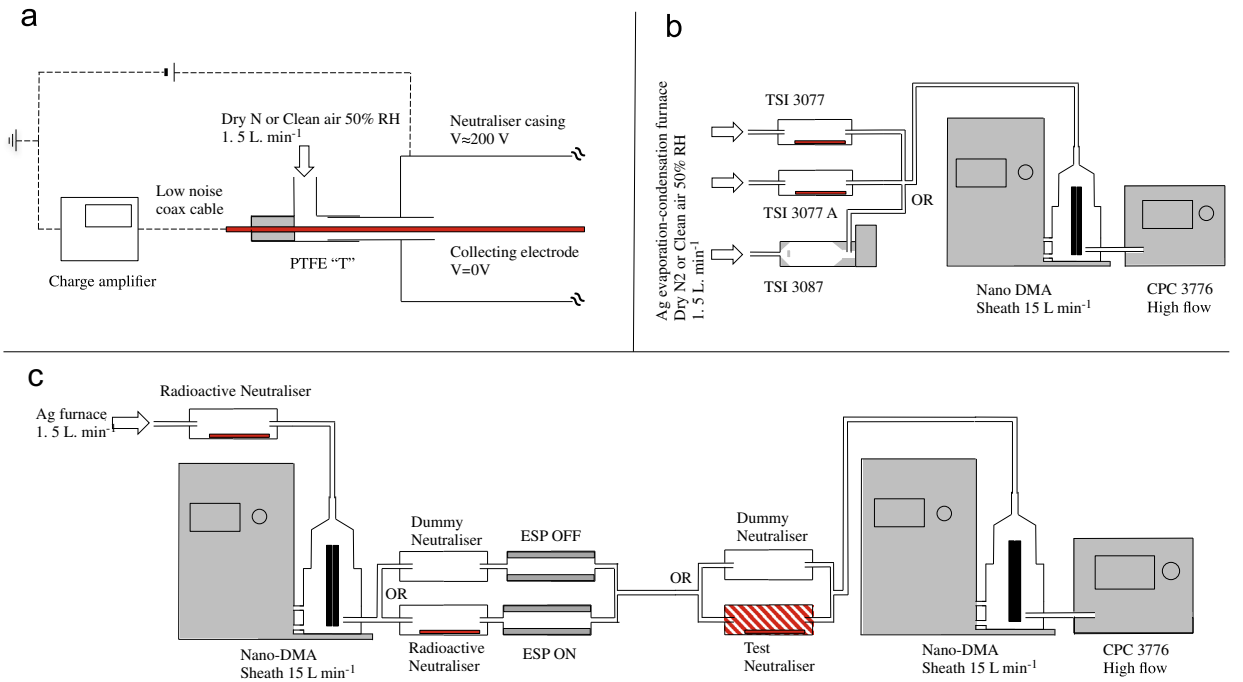


**Fig. 1.** Neutralisation of a polydisperse aerosol experiment set-up. Size distribution of the same aerosol is measured with a SMPS switching between the three neutralisers under study.

neutraliser. First, experimental evidence that the $n \cdot t$ product rule fails to predict neutraliser equilibrium behaviour is given. The aerosol charging equations for particles smaller than 35 nm diameter are then solved numerically, varying these four free parameters over a wide range of practically encountered situations. A non-dimensional analysis of the results subsequently enables mapping of equilibrium behaviour as a function of two non-dimensional groups, the non-dimensional ion concentration, and the non-dimensional neutraliser residence time. Agreement between theory and experiments is improved using a three-dimensional (3D) model accounting for charging inside the neutraliser. This work then discusses this as a new approach to non-equilibrium behaviour prediction in neutralisers, providing a tool supplementing the $n \cdot t$ product rule that can be used in practice.

## 2. Methods

### 2.1. Neutraliser characterisation

Experimental and simulation results presented in this work rely on three commercially available neutralisers, the TSI 3077A $^{85}$Kr neutraliser, with an estimated activity of 8 mCi; the TSI 3077 $^{85}$Kr neutraliser, with an estimated activity of 0.8 mCi; and the TSI 3087 Soft X-ray (SXR) neutraliser. Both $^{85}$Kr neutralisers have the same geometry, differing only by the strength of their ion generation rate, whereas the SXR has a similar total volume with different inlet and outlet design.

Neutraliser ion generation rates were measured experimentally by inserting a grounded electrode inside the ionisation chamber and applying a potential difference to the casing (Fig. 1a). A 1.5 L min$^{-1}$ HEPA-filtered gas stream flowed through the neutraliser and ions of a given polarity were attracted to the electrode. Assuming complete ion collection, the measured current in the rod was then used to derive the mean ion generation rate in the neutraliser, as shown by Liu and Pui (1974). In all experiments carrier gas was either dry nitrogen or a mixture of oxygen and nitrogen in proportions close to air composition, with 50% relative humidity.

### 2.2. Experimental evidence of non-equilibrium behaviour

The measured ion generation rate enabled the computation of $n \cdot t$ product values for the three neutralisers under study, where residence times are calculated assuming plug flow. In the light of these characteristic values, the experiment depicted in Fig. 1b allows for the assessment of the performance of the test neutralisers for neutralisation of a polydisperse aerosol. The study focused exclusively on quasi-spherical particles smaller than 35 nm diameter, which can only acquire a maximum of two net elementary charges by diffusion charging (Wiedensohler, 1988). The size distribution of the same test aerosol was measured several times with a SMPS, switching sequentially from one test neutraliser to the other to compare the $+1$ particle charge fractions at neutraliser outlet. For this purpose a polydisperse aerosol with geometric mean diameter around

**Table 1**
List of experimental situations studied with the non-dimensional approach.

| Experiment | Neutraliser | $N_{tot}$ [$m^{-3}$] |
|---|---|---|
| 1 | $^{85}$Kr 0.8 mCi | $4.9 \cdot 10^{10}$ |
| 2 | $^{85}$Kr 0.8 mCi | $5.1 \cdot 10^{11}$ |
| 3 | $^{85}$Kr 0.8 mCi | $1.1 \cdot 10^{13}$ |
| 4 | $^{85}$Kr 8 mCi | $4.9 \cdot 10^{10}$ |
| 5 | $^{85}$Kr 8 mCi | $5.1 \cdot 10^{11}$ |
| 6 | $^{85}$Kr 8 mCi | $1.1 \cdot 10^{13}$ |

15 nm, geometric standard deviation about 1.3 at total concentration about $10^{13}$ $m^{-3}$ was generated by evaporation-condensation of silver in a tube furnace at atmospheric pressure. Charged particles were removed using an electrostatic precipitator upstream of the test neutraliser. The particle size distribution was measured independently to ensure stability (less than 1% deviation in mean mobility diameter and less than 3% deviation in total particle concentration) during neutraliser testing. The test aerosol was sent to a TSI 3080 SMPS operated with one of the three test neutralisers. The SMPS consisted of a TSI 3085 NanoDMA with negative inner rod voltage and a TSI 3776 CPC in high-flow mode.

To measure charge fraction at the neutraliser outlet at lower total concentrations, a tandem mobility differential analysis (TDMA) set-up similar to Alonso, Kousaka, Nomura, Hashimoto, and Hashimoto (1997) was devised (Fig. 1c). Dummy neutralisers were used to measure total particle concentration downstream of the second DMA. The purpose of the first dummy neutraliser is to give the option to have only $+1$ or $-1$ charged particles entering the test neutraliser (ESP is turned off in this case), while taking diffusion losses into account. This can be used to (a) use initially $+1$ or $-1$ charged test particles for TDMA measurements, and (b) measure total particle concentration (Dummy neutraliser 1 → ESP off → Dummy neutraliser 2 → DMA 2 (same parameters as DMA1) → CPC).

The total particle concentration was maintained at $5 \cdot 10^{10}$ $m^{-3}$ ($\pm 3\%$) upstream of the test neutraliser, regardless of the particle size being tested. Unless stated otherwise, the monodisperse aerosol exiting the first DMA was neutralised using another neutraliser followed by an electrostatic precipitator.

In everything that follows experimental situations are numbered from 1 to 6 depending on the test neutraliser used, and the total particle concentration at the neutraliser inlet (Table 1). Unless stated otherwise particles entering the neutraliser were neutral, and the carrier gas was dry $N_2$ at a 1.5 L $min^{-1}$ flowrate.

### 2.3. One-dimensional charging model

In order to understand the influence of ion concentration, neutraliser residence time, total particle concentration, and particle size on the non-equilibrium behaviour of aerosol bipolar diffusion charging inside a neutraliser, it is first necessary to study a universal simplified model, whereby a monodisperse aerosol of given diameter and concentration is placed in an infinite uniform bipolar ionic atmosphere of a given ion concentration with fixed ion properties for a given time. When applying the model to a neutraliser, this interaction time can be understood as the residence time, equivalent to the axial distance along the neutraliser, hence the name one-dimensional model. However, in order to correctly describe charging inside a neutraliser, ion losses, velocity profile, and non-uniformity of the ion generation rate need to be included in the model, which is done in the three-dimensional model described in Section 2.5.

Microscopic interactions between gaseous ions and aerosol nanoparticles are described by collision kernels which account for the rate of collisions between the ion and the particle. Collision kernels were calculated following the method given by Reischl, Mäkelä, Karch, and Necid (1996), using Wiedensohler (1988) ion properties. Ion behaviour is governed by two ion properties, the ion mass and electrical mobility. These collision kernels can be applied to determine the macroscopic behaviour of a monodisperse aerosol of diameter $d_p < 35$ nm undergoing diffusion charging in a bipolar ionic atmosphere composed positive ions, concentration $n^+$, and negative ions, concentration $n^-$. Attachment coefficients between ions and particles are denoted $\beta_i^+(d_p)$ and $\beta_i^-(d_p)$, where $i$ is the net elementary charge of the particle. The concentration of $N_{\pm i}$ particles bearing $\pm i$ net elementary charges is described by the conservation of particle charge (Eq. (1)) and ions (Eq. (2)),

$$\frac{dN_{+i}}{dt} = n_+ N_{+i-1}\beta^+_{+i-1} + n_- N_{i+1}\beta^-_{+i+1} - n_+ N_{+i}\beta^+_{+i} - n_- N_{+i}\beta^-_{+i} \tag{1}$$

$$\frac{dn_j}{dt} = q - \alpha n_+ n_- - n_j(\beta^j_{+2}N_{+2} + \beta^j_{+1}N_{+1} + \beta^j_0 N_0 + \beta^j_{-1}N_{-1} + \beta^j_{-2}N_{-2}) \tag{2}$$

where $i$ is $-2$ to $+2$ and $j$ denotes either positive ($+$) or negative ($-$) charge. The ion generation rate, $q$, was measured experimentally for the test neutralisers. The ion–ion recombination constant, $\alpha$, was assumed to have an appropriate value for air ions in the concentration range found within the neutraliser, $\alpha = 1.6 \cdot 10^{-12}$ $m^3$ $s^{-1}$ (Hoppel & Frick, 1990). This one dimensional system of differential equations, along with the appropriate initial conditions, were solved numerically using MATLAB.

**Table 2**
Ranges of independent dimensional and dimensionless parameters tested.

| | Minimum | Maximum | Spacing | Datapoints |
|---|---|---|---|---|
| Dimensional | | | | |
| $q$ [$m^{-3} s^{-1}$] | $10^{11}$ | $10^{14}$ | Logarithmic | 50 |
| $N_{tot}$ [$m^{-3}$] | $10^{10}$ | $10^{14}$ | Logarithmic | 50 |
| $d_p$ [nm] | 4 | 35 | Logarithmic | 15 |
| $\tau_{res}$ [s] | 1 | 20 | Logarithmic | 50 |
| Dimensionless | | | | |
| $\hat{N}$ | −5 | 8 | – | 37,500 |
| $\hat{\tau}$ | 0.01 | 6 | – | 37,500 |

### 2.4. Equilibrium prediction via a non-dimensional approach

For a given ion generation rate ($q$), total particle concentration ($N_{tot}$), particle diameter ($d_p$), and neutraliser residence time ($\tau_{res}$), the relative difference to equilibrium levels in terms of +1 charge fraction ($f_{+1}^{Unsteady}$) can be described by the equilibrium indicator

$$J = \frac{f_{+1}^{Wied} - f_{+1}^{Unsteady}}{f_{+1}^{Wied}}, \tag{3}$$

where $f_{+1}^{Wied}$ is the equilibrium charge fraction of +1 charged particles predicted by Wiedensohler (1988) interpolation. $f_{+1}^{Wied}$ was chosen as the equilibrium reference as it is widely used in commercial SMPS systems. Different carrier gases compositions and flowrates will generate different ions in terms of electrical mobilities and masses, thus leading to different *equilibrium* charge distributions. Extensive work has been published on this subject by Kallinger et al. (2012), and Steiner and Reischl (2012). The latter demonstrate that for a wide range of experimentally measured ion properties, the relative uncertainty on positive equilibrium charge fractions remains below 6.5%. Using a single equilibrium fraction as a reference thus introduces a relative uncertainty of 6.5% on the quantity $J$.

The equilibrium behaviour described by $J$ for varying charging conditions can be described by the four governing parameters, $q$, $N_{tot}$, $d_p$, $\tau_{res}$. The four independent parameters with two dimensions (spatial and temporal) indicate that two non-dimensional groups may be formed to describe bipolar charging and provide an indication of charge equilibrium. Of the possible non-dimensional parameter formulations, the most appropriate dimensionless parameters represent the ratio of ion to particle concentration, $\hat{N}$, and ratio of residence time to characteristic charging time, $\hat{\tau}$, as defined in Eqs. (4) and (5), respectively.

$$\hat{N} \equiv \ln\left(\frac{n_0}{N_{tot} \cdot P_{coll}}\right) \tag{4}$$

$$\hat{\tau} \equiv \ln\left(\frac{\tau_{res}}{\tau_{char} \cdot f_{+1}^{Wied}}\right) \tag{5}$$

The ion concentration in the neutraliser without particles is given by $n_0 = \sqrt{q/\alpha}$, and the characteristic charging time is defined as $\tau_{char} = 1/(\beta \cdot n_0)$, where $\beta$ is the attachment coefficient of the average ion with a neutral particle. $P_{coll}$ is the probability of an average ion entering the limiting sphere colliding with the particle (see Hoppel and Frick (1986) for tables), and $f_{+1}^{Wied}$ the +1 equilibrium charge fraction predicted by Wiedensohler. For a detailed explanation of the concepts of limiting sphere, collision probabilities, and attachment coefficients, see Reischl et al. (1996). The dimensionless time and particle concentration were used to develop a functional relationship to the equilibrium indicator, $J = g\left(\hat{N}, \hat{\tau}\right)$, where the function, $g$, is to be determined.

To determine the functional relationship between $J$ and the independent parameters, the one-dimensional charging model was solved for 1.8 million iterations over relevant $\hat{N}$ and $\hat{\tau}$ for different sets of independent dimensional model parameters ($q$, $N_{tot}$, $d_p$ $\tau_{res}$). The ranges of the dimensional parameters investigated and corresponding non-dimensional values are shown in Table 2.

### 2.5. Three-dimensional charging model

The one-dimensional approach gives a universal insight into the relevant parameters to describe unsteady charging, however a 3D simulation is needed to fully capture the physics of the charging mechanisms occurring within neutralisers, including ion losses to the wall. For that purpose Eqs. (1) and (2) were solved in three spatial dimensions and one time dimension, using COMSOL. First, equations of mass and momentum conservation for an incompressible Newtonian fluid and a laminar flow were solved to compute the velocity and pressure fields, using the following boundary conditions of a fixed inlet flowrate of 1.5 L $min^{-1}$, atmospheric pressure, no viscous stress at neutraliser outlet, and no slip at neutraliser walls.

The velocity field, $\boldsymbol{u}$, was then used as an input to solve the ion and particle diffusion equations that account for charging

$$\nabla \cdot (-D_k \nabla c_k) + \boldsymbol{u} \cdot \nabla c_k = R_k \tag{6}$$

where $c_k$ and $D_k$ are the concentration and diffusion coefficient of species $k$, which is either an ion of a given polarity or a particle of a given charge. Again the aerosol was assumed to be monodisperse. $R_k$ is the production term that accounts for the charging phenomena, as described in the one-dimensional case (Eqs. (1) and (2)). The boundary conditions applied were an inflow of neutral particles at concentration $N_{tot}$ at the inlet, zero concentration of all species at neutraliser walls, and no outflow of particles at neutraliser inlet.

The ion generation term was taken as spatially unique, $q(x,y,z)$, for the radioactive neutralisers. Because the penetration range of beta particles is far greater than the neutraliser's characteristic dimension (Tsoulfanidis, 1995), it is assumed ion generation rate is uniform along their trajectories. Moreover, cloud chamber experiments suggest it is reasonable to approximate their trajectories as straight lines at these length scales. The non-uniformity is then only due to geometrical solid angle effects (Alonso & Alguacil, 2003),

$$q(x,y,z) = q_0 \cdot \alpha_1(x,y,z) \cdot \alpha_2(x,y,z) \tag{7}$$

where $\alpha_1(x,y,z)$ and $\alpha_2(x,y,z)$ are respectively the longitudinal and cross-sectional solid angles from which the source is seen at point $(x,y,z)$, described in SI 4, and $q_0$ is a constant adjusted so that the total ion generation rate integrated over the neutraliser is equal to the one that was measured experimentally. The SXR neutraliser has a similar ion generation rate mean value, however its geometrical distribution is thought to be much more uniform radially and longitudinally than for the radioactive neutralisers.

Detailed information about neutraliser geometries that were used in this study is available in SI 5.

For the 3D charging model a suitable metric for mean ion concentration was defined as the particle-averaged ion concentration. Results shown in Section 3.4 indeed show that ion and particle concentrations within the neutraliser are not homogeneous, which calls for the definition of a particle-averaged mean ion concentration instead of a volume averaged mean ion concentration. The mean ion concentration, $\overline{n_0}$, is determined by taking the ratio of the volume integral of the product of the local particle concentration and ion concentration terms to the product of total volume inlet particle concentration

$$\overline{n_0} = \frac{1}{V\, N_{tot}} \cdot \int\int\int \frac{\beta_0^+ n^+(x,y,z) + \beta_0^- n^-(x,y,z)}{\beta_0^+ + \beta_0^-} N(x,y,z)\,dx\,dy\,dz, \tag{8}$$

where $V$ is the volume of the neutraliser, $N_{tot}$ is the total particle concentration at the inlet, and $\beta_0^{\pm}$ is the attachment coefficients of a positive or negative ion with a neutral particle. $N(x,y,z)$ and $n^{\pm}(x,y,z)$ are the spatially dependent particle and ion concentrations, respectively. The resulting particle-averaged ion concentration can be thought of as the ion concentration in the vicinity of the particles.

## 3. Results

### 3.1. Neutraliser characterisation

Table 3 summarises the relevant characteristics of the three neutralisers considered. The total ion generation rate of the strong radioactive neutraliser is an order of magnitude higher than that of the weak radioactive neutraliser, which compares well with those found in the literature (Lee, Soo Kim, Shimada, & Okuyama, 2005). The total ion generation rate of the SXR charger was measured to be $2 \cdot 10^{13}$ m$^{-3}$ s$^{-1}$, a value of the same order of magnitude than what was previously measured in the literature for similar chargers (Lee et al., 2005; Yun, Lee, Iskandar, Okuyama, & Tajima, 2009). Carrier gas composition seems to have only a marginal effect on ion generation rate. The $n \cdot t$ product values were calculated using the assumptions of plug flow and uniformly distributed ion generation rate. Although all three neutralisers have a $n \cdot t$ product greater than $10^{13}$ m$^{-3}$ s, which is the minimum value given by the ISO standard (BS ISO 15900:2009(E), 2009), it will be shown in the next section that they all display non-equilibrium behaviour under certain circumstances.

**Table 3**
Neutraliser measured total ion generation rate $q$, and $n \cdot t$ product for a flowrate of 1.5 L min$^{-1}$ assuming plug flow.

| Carrier gas | | TSI 3077 $^{85}$Kr 0.8 mCi | TSI 3077A $^{85}$Kr 8 mCi | TSI 3087 SXR |
|---|---|---|---|---|
| Dry $N_2$ | $q$ [m$^{-3}$ s$^{-1}$] | $9.1 \cdot 10^{12}$ | $1.3 \cdot 10^{14}$ | $2.0 \cdot 10^{13}$ |
| Air 50% RH | $q$ [m$^{-3}$ s$^{-1}$] | $9.4 \cdot 10^{12}$ | $1.3 \cdot 10^{14}$ | $2.3 \cdot 10^{13}$ |
| Dry $N_2$ | $n.t$ [m$^{-3}$ s] | $1.7 \cdot 10^{13}$ | $6.3 \cdot 10^{13}$ | $3.2 \cdot 10^{13}$ |
| Air 50% RH | $n.t$ [m$^{-3}$ s] | $1.7 \cdot 10^{13}$ | $6.3 \cdot 10^{13}$ | $3.2 \cdot 10^{13}$ |

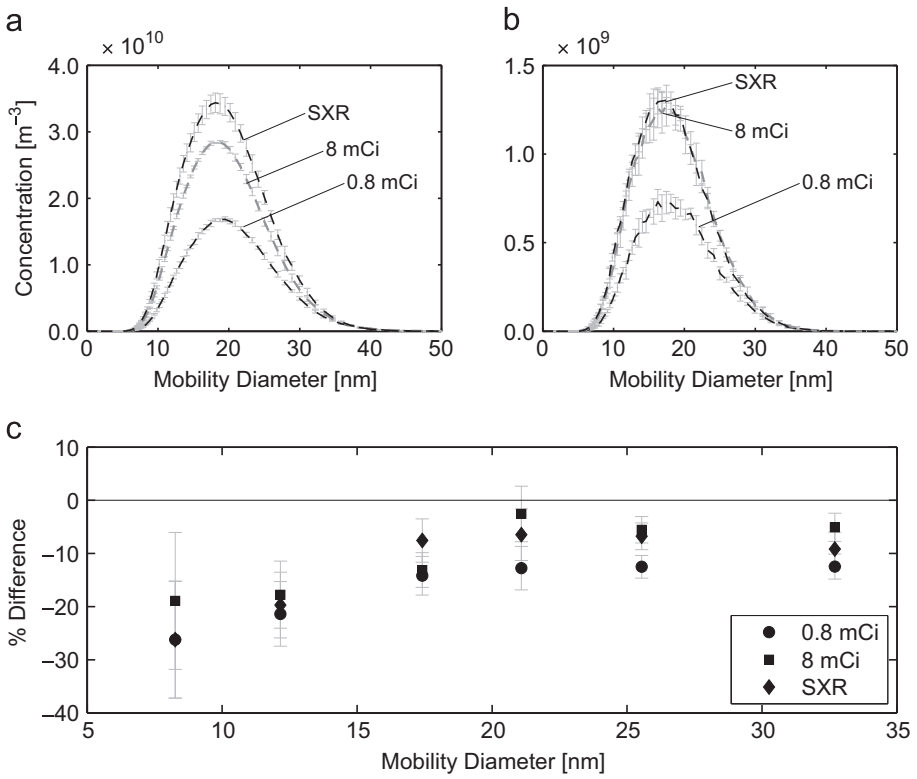


**Fig. 2.** SMPS size distributions a constant aerosol source of concentration: (a) $N_{tot} = 10^{13}$ m$^{-3}$ and (b) $N_{tot} = 5 \cdot 10^{10}$ m$^{-3}$ using $^{85}$Kr 0.8 mCi, $^{85}$Kr 8 mCi and SXR neutralizers. Error bars represent a 95% confidence interval based on the standard deviation of twelve two minutes measurements. (c) TDMA measurements of $+1$ charge fraction for $^{85}$Kr 0.8 mCi, $^{85}$Kr 8 mCi and SXR neutralizers, per cent difference to Wiedensohler $+1$ charge fraction, $\%\Delta W = (f_{+1}^{Exp} - f_{+1}^{Wied})/f_{+1}^{Wied}$. Error bars represent a 95% confidence interval based on the standard deviation of 12 measurements for each mobility diameter. In all cases particles entering the neutraliser were initially neutral.

### 3.2. Experimental evidence of non-equilibrium behaviour

Fig. 2 shows the raw concentrations given by the CPC when the size distribution of the same, initially neutral aerosol was measured with the SMPS using three test neutralisers. For all other parameters held constant, the higher particle raw counts means that the $+1$ charge fraction at the outlet of the test neutraliser is higher. At a high total particle concentration (Fig. 2a), all three neutralisers produce different $+1$ charge fractions. As expected from ion generation rate measurements, the $^{85}$Kr 0.8 mCi radioactive neutraliser gives the lowest $+1$ charge fraction. Surprisingly the SXR charger gives a higher $+1$ charge fraction than the $^{85}$Kr 8 mCi radioactive neutraliser, despite having a lower ion generation rate and $n \cdot t$ product. When total particle concentration is lowered (Fig. 2b) both of the neutralisers with the highest ion generation rate are in agreement, while the $+1$ charged fraction given by the weak, $^{85}$Kr 0.8 mCi radioactive neutraliser remains $\sim$50% lower. For lower particle concentrations ($< 10^{10}$ m$^{-3}$, Fig. 2c), all three neutralisers agree within the measurement error.

TDMA measurements shown in Fig. 3 indicate for initially $+1$ charged particles entering the test neutraliser at a concentration of $10^{10}$ m$^{-3}$ results in varying differences to Wiedensohler-predicted charge. The $^{85}$Kr 0.8 mCi charger shown in Fig. 3a is unable to neutralize the test aerosols resulting in a net positive charge for the aerosol at all tested mobility diameters. The greater ion generation rate of the 8 mCi $^{85}$Kr and SXR neutralizers better able to neutralize the test aerosol, resulting in neutral, $+1$ and $-1$ charged fractions that are in better agreement with steady-state charging as indicated by the Wiedensohler lines. Despite the better performance of the higher ionising sources, the relative difference between the $+1$ charge fraction predicted by Wiedensohler and the measured charge (Fig. 3d) is as great as 160% and 70% for the 8 mCi $^{85}$Kr and SXR neutralizers, respectively. The radioactive neutralizers demonstrate an increased error at small particle sizes which tends to decrease for larger diameters, whereas the SXR shows an increase in error at large particle diameters. These measurements indicate that despite the "sufficient" $n \cdot t$ product of all neutralizers there appear to be cases where a steady-state charge distribution is not achieved. Clearly, initial charge is an aggravating factor for non-equilibrium behaviour of neutralisers. The rest of this work focuses on initially neutral particles, but a similar non-dimensional approach could be used for initially charged aerosols, provided space charges are included in the models.

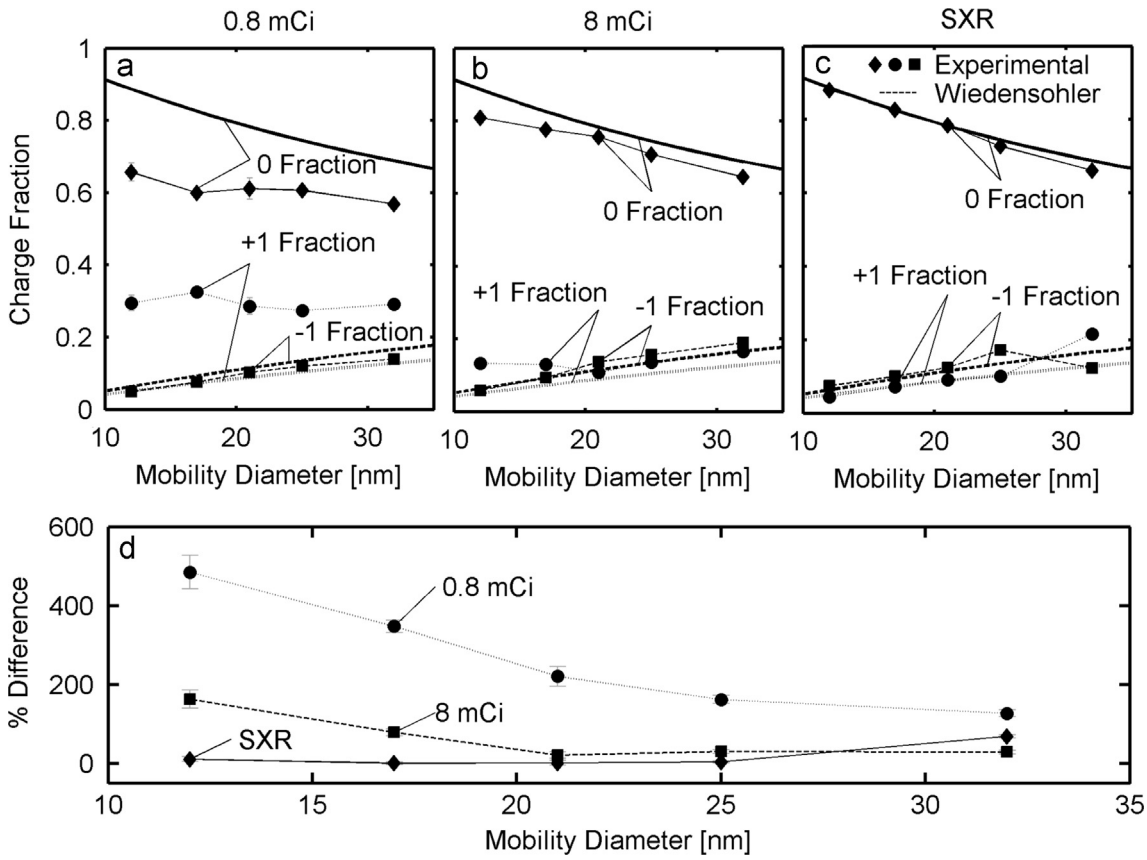


**Fig. 3.** TDMA measurements of +1, −1 and neutral charge fractions for: (a) $^{85}$Kr 0.8 mCi, (b) $^{85}$Kr 8 mCi, (c) SXR neutralizers and (d) relative difference to Wiedensohler +1 charge fraction, $\Delta W = (f_{+1}^{Exp} - f_{+1}^{Wied})/f_{+1}^{Wied}$. Error bars represent a 95% confidence interval based on the standard deviation of 12 measurements for each mobility diameter. In all cases particles entering the neutraliser were initially +1 charged.

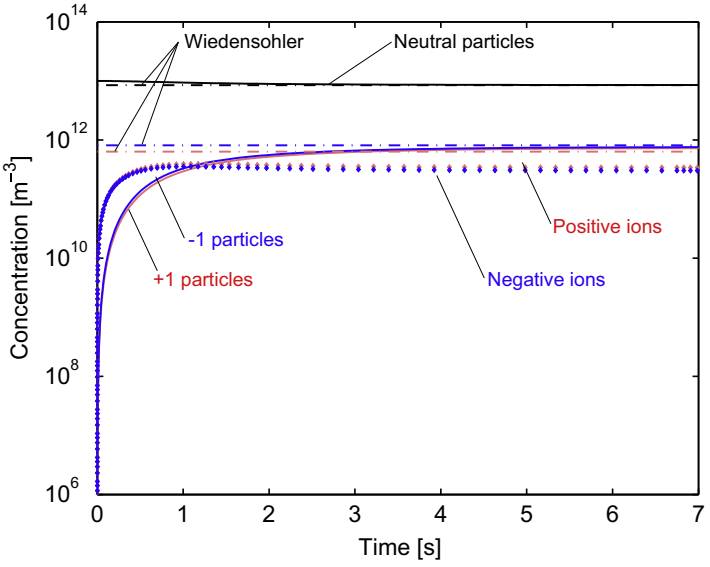


**Fig. 4.** Typical neutraliser temporal charging curve for positive, negative and neutral particles. Specific model constants are $D_p = 15$ nm, $N_{tot} = 10^{13}/m^3$, $q = 10^{12}/m^3/s$, Wiedensohler ions.

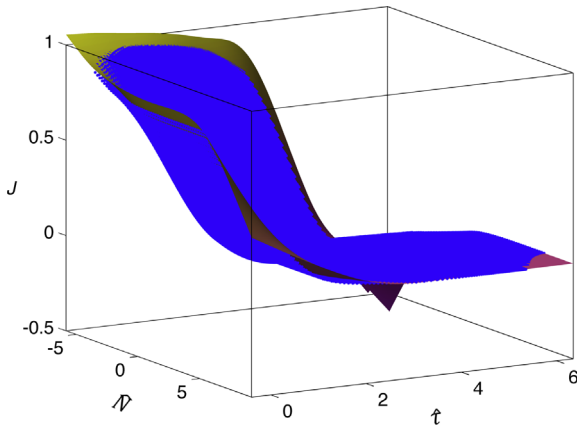


**Fig. 5.** Numerically-determined equilibrium indicator $J$ (blue dots) calculated by the 1-D charging model plotted against the non-dimensional concentration, $\hat{N}$, and residence time, $\hat{\tau}$, which represent the range of dimensional model variables described in Table 1. An interpolated surface with good fit to the data ($R^2$=0.985) is also shown. (For interpretation of the references to colour in this figure legend, the reader is referred to the web version of this article.)

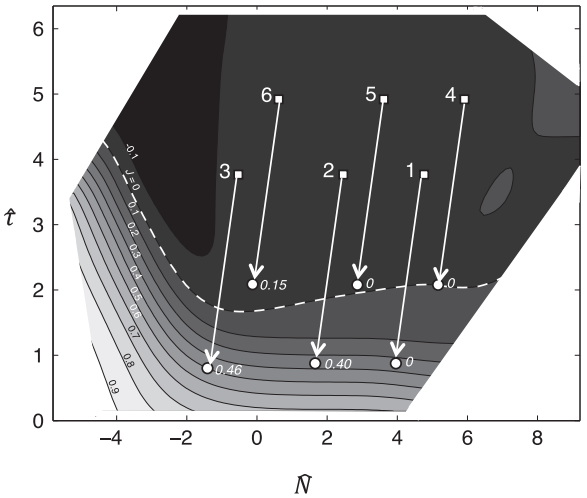


**Fig. 6.** Contour levels of the interpolated surface displayed in Fig. 4, where equilibrium indicator $J$ as a function of non-dimensional concentration, $\hat{N}$, and residence time, $\hat{\tau}$. Dashed line is contour level $J$=0 that delimits the region between equilibrium and transient behaviour. Squares are experimental results for the radioactive neutralisers described in Fig. 2. In each case $\hat{N}$ and $\hat{\tau}$ were computed assuming plug flow and a uniform ion generation rate within the neutraliser equal to the one that was measured experimentally. The arrows and circles represent the correction when correct values $\overline{n_0}$ and $\overline{\tau_{res}}$ from the 3-D charging model are used to compute $\hat{N}$ and $\hat{\tau}$. The figures next to the circles represent the experimentally-measured $J$ level The experimental datapoints are (1) 0.8 mCi $^{85}$Kr neutraliser, $N_{tot}=5\cdot10^{10}$ m$^{-3}$; (2) 0.8 mCi $^{85}$Kr neutraliser, $N_{tot}=5\cdot10^{11}$ m$^{-3}$; (3) 0.8 mCi $^{85}$Kr neutraliser, $N_{tot}=10^{13}$ m$^{-3}$; (4) 8 mCi $^{85}$Kr neutraliser, $N_{tot}=5\cdot10^{10}$ m$^{-3}$; (5) 8 mCi $^{85}$Kr neutraliser, $N_{tot}=5\cdot10^{11}$ m$^{-3}$; and (6) 8 mCi $^{85}$Kr neutraliser, $N_{tot}=10^{13}$ m$^{-3}$.

### 3.3. Equilibrium prediction via a non-dimensional approach

A typical neutraliser charging curve given by the 1D model described above is displayed in Fig. 4. With ion properties equivalent to those used by Wiedensohler, the charge fractions converge as expected to their equilibrium value predicted by the Wiedensohler interpolation. The time required to reach convergence (defined as 5% difference) to Wiedensohler charge fractions is 2.9 s. Ion equilibrium concentrations result from a balance between production from the source described by the ion generation rate and losses to the particles and ion–ion recombination. As a result of their greater mobility, the negative ions have a lower steady-state concentration and the fraction of negative particles is greater than the positive fraction. The time to reach the equilibrium charge distribution increases as the particle concentration increases and decreases with increased mean aerosol mobility diameter and ion generation rate.

Fig. 5 displays equilibrium indicators, $J$, plotted (blue dots) for varying non-dimensional concentration, $\hat{N}$, and residence time, $\hat{\tau}$, as computed by the 1D-charging model over the ranges of dimensional variables shown in Table 2. As shown, the equilibrium indicator is a smooth function of $\hat{N}$ and $\hat{\tau}$, indicating that the dimensionless formulations of $\hat{N}$ and $\hat{\tau}$ are robust over the wide range of dimensional values used within the model. Multiple combinations of input values for $q$, $N_{tot}$, $d_p$ and

**Table 4**
SXR charger output charge fractions as computed by the axisymmetric COMSOL model for a flow flowrate of 1.5 L min$^{-1}$ with initially neutral $d_p$=15 nm particles.

| $N_{tot}$ [m$^{-3}$] | $f_{+1}$ [%] | $f_{-1}$ [%] |
|---|---|---|
| $4.9 \cdot 10^{10}$ | 5.11 | 6.50 |
| $5.1 \cdot 10^{11}$ | 5.11 | 6.50 |
| $1.1 \cdot 10^{13}$ | 5.11 | 6.50 |
| Wiedensohler | 6.36 | 8.13 |

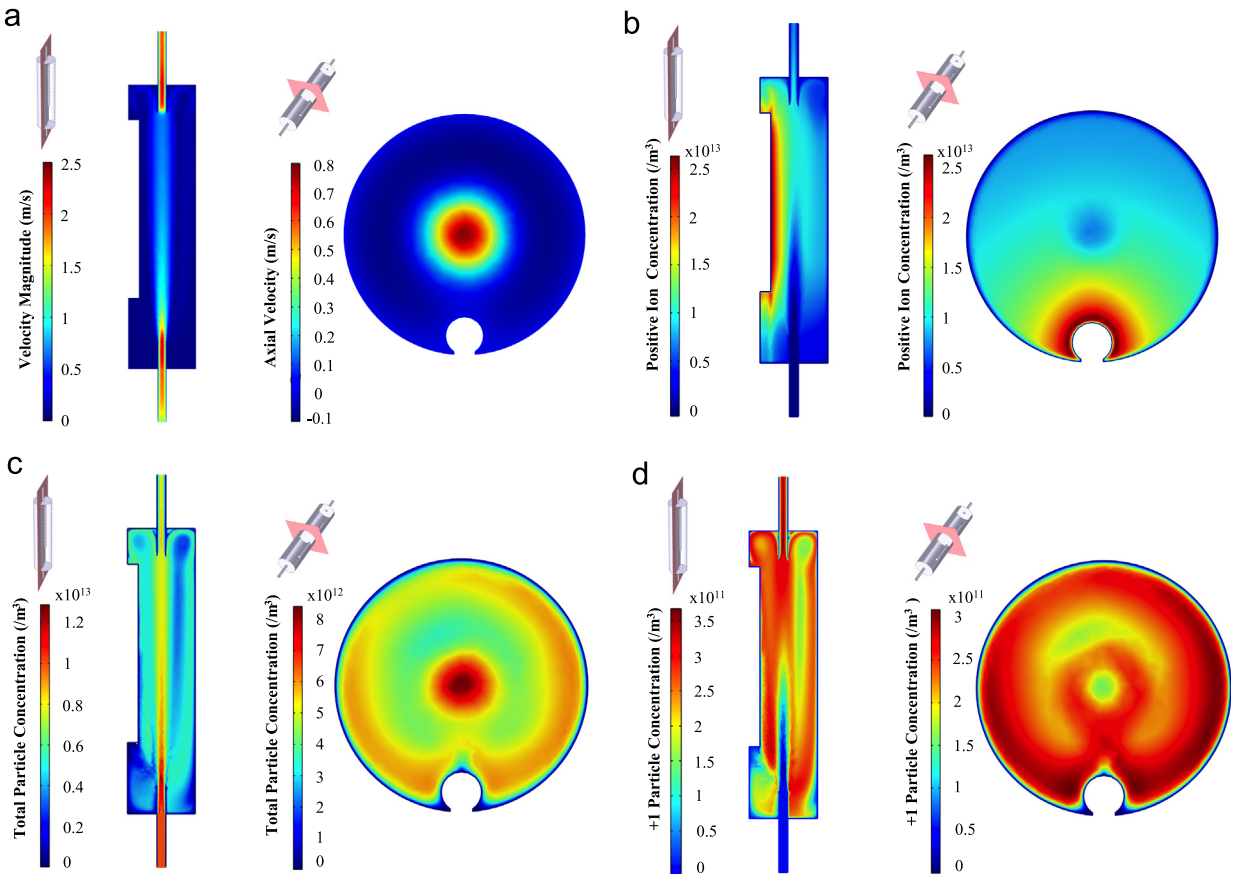


**Fig. 7.** (a) Velocity field within TSI 3077 neutraliser operated at a flowrate of 1.5 L min$^{-1}$ Positive ion (b), total particle (c), and +1 particle (d) concentrations within TSI 3077 neutraliser operated at a flowrate of 1.5 LPM, with a total concentration $N_{tot}$=$10^{13}$/m$^3$ of initially neutral $D_p$=15 nm monodisperse particles at the inlet. Longitudinal cross-section: inlet at the bottom, radioactive source on the left. Cross-sectional view: radioactive source at the bottom.

$\tau_{res}$ may result in the same $\hat{N}$ and $\hat{\tau}$, which in turn result in the same degree of charge equilibrium, thus demonstrating the validity of the dimensionless group formulations. The tight planar distribution of $J$ allows for an interpolated surface to be fit to the data points resulting in a 3D surface function (see SI 1) that agrees with the numerical data points ($R^2$=0.985). The resulting surface demonstrates that as $\hat{N}$ and $\hat{\tau}$ increase (increased relative ion concentration and residence times, respectively) the equilibrium is approached ($J$ approaches zero).

Fig. 6 shows the contours of the interpolated surface as a function of $\hat{N}$ and $\hat{\tau}$. The dashed line follows the contour $J$=0, which represents the limit between equilibrium (above and right of this line) and transient behaviour (below and left of this line). The shape of the $J$=0 contour is as expected: to reach equilibrium a large value of $\hat{N}$ is needed in case of a small value of $\hat{\tau}$. A functional fit for $J$=0 is given by the relation

$$\hat{\tau} = \sum_{i=1}^{6} a_i \cdot \hat{N}^i \tag{9}$$

with $a_1 = 1.05 \cdot 10^{-5}$, $a_2 = -1.432 \cdot 10^{-4}$, $a_3 = 3.658 \cdot 10^{-4}$, $a_4 = 3.43 \cdot 10^{-3}$, $a_5 = -2.686 \cdot 10^{-2}$, $a_6 = 1.671$ for $-4 < \hat{N} < 7$. This contour is not a straight line, as would be indicated by the $n \cdot t$ product rule. Clearly this new approach, based on the map of $J$, captures the influence of total particle concentration and particle size.

The squares represent the experimental results for the strong and weak radioactive neutralisers described in Fig. 2. In each case $\hat{N}$ and $\hat{\tau}$ were computed assuming plug flow and a uniform ion generation rate within the neutraliser as determined experimentally. The surface of the function can be used to predict the equilibrium level of experimental data provided that the appropriate $\hat{N}$ and $\hat{\tau}$ can be determined. As an example, Square 3 representing a 0.8 mCi $^{85}$Kr neutraliser with a concentration of $N_{tot} = 10^{13}$ m$^{-3}$ lies in an area where the equilibrium function of $\hat{N}$ and $\hat{\tau}$ predicts $J$ to be near zero ($J = -0.04$), e.g. near equilibrium. However, Fig. 2a shows that for these conditions, the value of equilibrium was experimentally measured to be $J = 0.46$. These results indicate that when determining the non-dimensional parameters $\hat{N}$ and $\hat{\tau}$ for experimental systems, simplifications do not account for 3D behaviour, such as assuming the residence time can be determined using plug flow or that the ion concentration is uniformly equivalent to $n_0 = \sqrt{q/\alpha}$. Therefore, to apply the equilibrium indicator, as determined by the one-dimensional charging model, appropriate variable averages must be used to form the non-dimensional parameter values. These corrected ($\hat{N}$ and $\hat{\tau}$) values are depicted by the arrows and circles on Fig. 6, whereby the next section explains how these corrections were determined. The figures next to these circles represent the experimentally measured $J$ where the equilibrium $+1$ charge fraction is given by the SXR charger, as justified below.

### 3.4. A three-dimensional charging model to calculate relevant $\hat{N}$ and $\hat{\tau}$ values

The model was first validated in an axisymmetric configuration (see SI 5) with a spatially uniform ion generation rate, in order to account for neutralisation in the SXR charger. The value of the ion generation rate was equal to the one that was measured experimentally. For the SXR charger, outlet charge fractions were found to reach equilibrium levels in all situations described in Table 1. That is, for $d_p = 15$ nm particles and a flowrate of 1.5 L min$^{-1}$, outlet charge fractions do not depend on total particle concentration in the range $N_{tot} = 5 \cdot 10^{10}$ m$^{-3}$–$10^{13}$ m$^{-3}$, and are within a 20% range of the charge fractions predicted by Wiedensohler, as can be seen in Table 4. It was found that by tuning the values of ion masses and mobility within a realistic range it was possible to reach charge distributions very close to Wiendensohler interpolation. For instance ($Z^+ = 1.6$ cm$^2$ V$^{-1}$ s$^{-1}$, $Z^- = 2.1$ cm$^2$ V$^{-1}$ s$^{-1}$, $m^+ = 166$ a.m.u., $m^- = 110$ a.m.u.) yields ($f_{+1} = 6.2\%$, $f_{-1} = 7.8\%$), to be compared with Table 4. This is of no concern for the model, as it does not aim at quantitatively predicting outlet charge fractions, but at computing the $\hat{N}$ and $\hat{\tau}$ values, which are more robust parameters whose sensitivity to ion property changes is negligible for the purpose non-dimensional approach to equilibrium prediction. In the rest of this work ion properties are fixed to Wiedensohler (1988) properties.

Moreover, the fact that the SXR charger produces equilibrium level charge fractions in all of the situations described above can also be predicted by the non-dimensional approach previously outlined, using results from the one-dimensional model only: assuming a uniform ion generation rate $q = 2 \cdot 10^{13}$ m$^{-3}$ s$^{-1}$, for a total particle concentration $N_{tot} = 10^{13}$ m$^{-3}$ (worst case scenario in this work), and with a residence time $\tau_{res} = 1$ s (worst case scenario for a 1.5 L min$^{-1}$ flowrate as explained in Section 4.1), Eqs. (4) and (5) yield $\hat{N} = -0.18$ and $\hat{\tau} = 2.13$. Looking at Fig. 6 it can be seen that for those values of $\hat{N}$ and $\hat{\tau}$, $J = 0$. This confirmed that the COMSOL model was correctly implemented and that the SXR charger could be thought of as a reference neutraliser that gives equilibrium charge fractions in all the situations studied in this work.

Fig. 7 displays the flow field and ion and particle concentrations within the 0.8 mCi $^{85}$Kr neutraliser operated at a flowrate of 1.5 L min$^{-1}$, with a total concentration $N_{tot} = 10^{13}$ m$^{-3}$ of initially neutral $d_p = 15$ nm monodisperse particles at the inlet. The velocity flow field (Fig. 7a) demonstrates that the majority of the flow is confined to the central region of the neutraliser with a large surrounding dead volume consisting of recirculation zones. Most of the particles (Fig. 7c), remain confined in a central "jet" with little radial diffusion, thus lowering their residence time within the neutraliser. Conversely, most of the ions (Fig. 7b) remain confined close to the source due to the higher ion generation near the source and flow recirculation regions. Ions diffuse away from the source, but the convection of the central flow jet is such that their concentration remains low in the region where particle concentration is highest, e.g. the average ion concentration is $1.4 \cdot 10^{12}$ m$^{-3}$ along the centreline of the neutraliser. As expected, neutral particle concentration is high in the central jet as the aerosol encounters relatively few ions, with a very short residence time. Charged particles are highest (Fig. 7d) in the recirculation regions as they become charged due to the relatively higher ion concentration and longer residence time.

From these results it is clear that $\hat{N}$ and $\hat{\tau}$ cannot be calculated assuming plug flow to calculate residence time, $\tau_{res}$, and a uniform ion generation rate to estimate $n_0 = \sqrt{q/\alpha}$. Instead, the particle-averaged residence time, $\overline{\tau_{res}}$, and the particle-weighted ion concentration, $\overline{n_0}$, were defined to better represent 3D behaviour. The particle-averaged residence time was computed numerically by sending a burst of particles inside the neutraliser and monitoring the outlet concentration (Levenspiel, 1998). The resulting average particle residence time was determined to be $\overline{\tau_{res}} = 1$ s for both radioactive neutralizers (same geometry and volumetric flow rate). A video of this process is provided in supplementary information 2.

Supplementary material related to this article can be found online at http://dx.doi.org/10.1016/j.jaerosci.2015.03.006.

The particle weighted-ion concentration was numerically calculated in accordance with Eq. (8) for the 0.8 mCi $^{85}$Kr neutraliser with varying inlet particle concentrations ranging from $5 \cdot 10^{10}$ m$^{-3}$ to $10^{13}$ m$^{-3}$, which resulted in particle average ion concentration of $\overline{n_0} = 10^{12}$ m$^{-3}$ $\pm$ 10%, nearly independent of initial particle concentration. For the 8 mCi $^{85}$Kr neutraliser the particle-average ion concentration was found to be $\overline{n_0} = 3.7 \cdot 10^{12}$ m$^{-3}$ $\pm$ 2%, and nearly independent of initial

particle concentration. The robustness of the $\overline{n_0}$ values to differing particle concentrations indicates that the particle-average ion concentration is determined more by the strength of the neutraliser than the loss of ions to the particles.

The values of $\overline{\tau_{res}}$ and $\overline{n_0}$ calculated using the 3D model were then applied to determine $\hat{N}$ and $\hat{\tau}$, yielding the corrected data represented by the circles in Fig. 6. The 3D determined parameters improved the agreement between the non-dimensional approach and the experimental results. Points 2 and 3 lie below the $J=0$ line, and Points 4 and 6 lie above the line, as expected by the experimental measurements. Point 1 lies within the $J=0.15$ region whereas experimental measurements indicate it should lie in the $J=0$ region. Conversely, Point 6 lies within a $J=0$ line whereas experiments suggest that it should be near the $J=0.15$ region. A factor that may contribute to the experimental error is the assumption that the SXR charger gives equilibrium level of $+1$ charge fraction. Considering the negative $J$ value in this area of the map it is possible that the SXR charger actually yields a $+1$ charge fraction greater than equilibrium levels, hence explaining the relatively lower $+1$ charge fraction given by the strong radioactive neutraliser.

## 4. Discussion

### 4.1. $\hat{N}$ and $\hat{\tau}$ as new equilibrium indicators

Results indicate $\hat{N}$ can be thought of as the non-dimensional ion concentration; the relevant ion concentration to reach equilibrium cannot be absolute and must be compared to the total particle concentration. This non-dimensional ion concentration is particle size dependent via the collision probability, $P_{coll}$, which increases with particle size. For large particles, more ions will be lost to particles and therefore more ions are necessary to reach equilibrium. $\hat{\tau}$ can be thought of as the non-dimensional particle residence time in the neutraliser. Its relevance stems from the relationship between the characteristic time for charging, $\tau_{char}$, and residence time, where $\tau_{char}$ depends on particle size and ion concentration. For conditions where ion–particle collision are very scarce (i.e. very large characteristic charging time), a longer interaction time is required to reach equilibrium. The $f_{Wied}$ factor in the denominator reflects the higher equilibrium charge fractions for larger particles that need more ion–particle collisions for equilibrium to be achieved, and therefore a longer time in the neutraliser. The overall impact of particle diameter serves to increase $\beta$ ($\hat{\tau}$ numerator) and $f_{+1}^{Wied}$ ($\hat{\tau}$ denominator) with a resulting net increase in $\hat{\tau}$ with increased particle diameter for the range of diameters concerned within this study (see SI 6).

The interpolated surface that represents $J$ (see Fig. 6) is negative in a region with small $\hat{N}$ and large $\hat{\tau}$, that is the $+1$ charge fraction is higher than equilibrium in a region where the relative concentration of ions to particles is low and where the residence time is long. Analysis of the 1D simulations in these situations suggests this is due to the ratio of positive to negative ion concentration being significantly greater than unity: as negative ions are more mobile they are more easily lost to particles and walls. When $\hat{N} < -1$, that is when ion concentration is about one order of magnitude lower than particle concentration for 15 nm diameter particles, the time to reach equilibrium increases significantly. Even when the 3D corrections of particle-weighted ion concentration are used, experiments suggest that the influence of particle concentration starts to be significant for even lower particle to ion ratios (see Fig. 2b). This discrepancy may be due to the difference in particle dispersity between the experiment (polydisperse) and the model (monodisperse). It was not possible to provide mono-mobility particles to the test neutraliser with sufficiently high concentrations to make a direct experimental comparison to the model.

Agreement between experiments and predictions on equilibrium behaviour based on the map of $J$ using the 3D model to calculate $\hat{N}$ and $\hat{\tau}$ values is sufficient to indicate that the method can be used as a conservative equilibrium predictor. As the current formulation tends to slightly overestimate the non-equilibrium behaviour (cf. Fig. 6, Point 1), thus indicating that the $J=0$ line provides an inherent safety margin. In practice, the value of $\hat{N}$ and $\hat{\tau}$ should be calculated according to the charging situation accounting for neutraliser design, and the functional fit of the $J=0$ contour can then be used to determine whether or not equilibrium is reached inside the neutraliser. If the ($\hat{N}$, $\hat{\tau}$) data point lies below or left of the $J=0$ contour, then equilibrium will not be reached and alternative strategies must be developed to interpret SMPS data. Thus, values of $\overline{\tau_{res}}$ and $\overline{n_0}$ need to be calculated from the flowrate and total ion generation rate values, which can easily be measured or estimated. In this study, values of $\overline{\tau_{res}}$ and $\overline{n_0}$ were derived using the 3D charging model, which may not be practical for all measurements.

The values for $\overline{\tau_{res}}$ and $\overline{n_0}$ can be determined by multiple methods. $\overline{\tau_{res}}$ values could be derived using CFD, or measured experimentally using a tracer step experiment and laminar reactor residence time distribution theory (Levenspiel, 1998). For tracer measurements a stable source and a detector with fast response time relative to neutraliser residence time is required. Unfortunately even the fastest commercially available CPCs do not allow this measurement with aerosol as the tracer. CPC response time to a step is $\sim$1 s, which is of the order of the neutraliser residence time in the case of a TSI 3077 neutraliser at 1.5 L min$^{-1}$. Using a tracer gas like $CO_2$ and an ultrafast gas sensor might be a solution. Even though $CO_2$ molecules and aerosol particles do not have the same diffusion coefficient, CFD calculations suggest the difference in measured residence time is insignificant ($<3\%$). Alternatively, a worst-case scenario correction factor could be used to relate residence time calculated assuming plug flow $\tau_{plug}$ and $\overline{\tau_{res}}$. In the case of the TSI 3077 neutraliser, CFD simulations using the 3D model suggest that $\overline{\tau_{res}} > 0.1\tau_{plug}$ in the flowrate range 0.3–1.5 L min$^{-1}$ with a worst case scenario being a flowrate of 0.3 L min$^{-1}$. However it must be emphasised that the value of $\overline{\tau_{res}}$ represents the quality of the mixing occurring in the neutraliser and is therefore sensitive to disturbances in the flow upstream of the neutraliser, such as mixing orifices. Ultimately an experimental method would therefore be best to determine $\overline{\tau_{res}}$.

A similar approach may be applied to the determination of $\overline{n_0}$. Ideally it should be related to the experimentally-measured ion generation rate $q$ using a 3D model, which takes the non-uniformity of the ion generation rate into account. In the case of the TSI 3077 neutraliser geometry, using the 3D charging model it was found that for a range of flowrates (0.3–1.5 L $min^{-1}$), a range of measured ion generation rate $q$ ($10^{12}$–$10^{14}$ $m^{-3}s^{-1}$) and a range of particle concentration ($10^{11}$–$10^{13}$ $m^{-3}$), the resulting relation can be used $\overline{n_0} \approx 0.41\sqrt{q/\alpha}$ to determine $\overline{n_0}$ within 8%. As shown in supplementary information 3, these results are very weakly dependant on particle concentration, flowrate, and ion generation rate. Neutraliser manufacturers could provide this correction factor as evidence for the good mixing performances of their neutraliser.

### 4.2. The 3D charging model: a useful insight for neutraliser design

Charge fractions at the neutraliser outlet as computed directly from the 3D model are very dependent on ion properties. It must be emphasised that the Wiedensohler (1988) ions used in this study are not necessarily representative of the real ions found in the neutralisers. Various studies show that different neutralisers will generate different ions under different carrier gas conditions (Steiner & Reischl, 2012), and that the complex ion spectrum actually depends on the whole system used, including the choice of tubing material upstream of the neutraliser (Steiner et al., 2014; Steiner & Reischl, 2012). While this might not be a significant problem for equilibrium charge fraction prediction (Steiner & Reischl, 2012), this uncertainty has consequences on the unsteady 3D model presented in this work, where the ion diffusion coefficient directly influences ion losses to the wall. Moreover, Wiedensohler ion properties were selected to best fit experimental results on equilibrium charge fractions, and do not result from a single, direct measurement. Over the years Wiedensohler ion properties have been shown to be extremely robust to predict equilibrium levels in a wide range of experimental situations, but again the 3D model described in this work demands physically relevant values. Lastly, even if the exact ion spectrum was measured in all experimental situations studied here, only one positive ion and one negative ion are used in the simulation. More fundamental work is needed to determine what the properties of these ions should be relative to the full spectrum. For instance it is possible that the most abundant ion does not account for the majority of the charging, but rather charging is dominated by more mobile, less abundant ions. By tuning ion properties within the 3D simulation to values that remain physically reasonable, it is possible to reach absolute agreement between direct 3D simulations and experiments for $+1$ charge fraction calculation. This should not be interpreted as the correct value for ion mobility and masses, as too many assumptions are made in the model to have quantitative direct predictions: monodisperse aerosol, inlet velocity profile, neutraliser geometry, geometry of the ion generation rate, negligible space charge effects. Fortunately the non-dimensional approach, along with the computation of $\overline{\tau_{res}}$ and $\overline{n_0}$ is sufficiently robust to enable predictions of the equilibrium behaviour to be made in practice.

Aerosol devices such as chargers or coagulation chambers are often modelled as a uniform medium, but output from the 3D charging model shows that this is not the case. It is clear that neutraliser equilibrium behaviour is dominated by its mixing performances: the particle averaged residence time $\overline{\tau_{res}}$ needs to be maximised for a given flowrate, and the particle weighted ion concentration $\overline{n_0}$ needs to be maximised for a given total ion generation rate. The control of the flow and control of the ion generation rate spatial distribution can be used to maximise these parameters. $\overline{\tau_{res}}$ can be optimised either by achieving fully-developed flow inside the ionisation chamber, or by disturbing the flow to get rid of the central jet described above. In both cases, design of the inlet is critical, where a tapered inlet, a mixing orifice, or an obstacle to the flow can serve to enhance mixing, as in the TSI 3087 SXR charger. $\overline{n_0}$ can be optimised by having the ion generation rate stronger where most of the particles are located. Having a uniform ion generation rate distribution, as for the SXR charger, is shown to have increased particle weighted ion concentrations.

## 5. Conclusion

The $n \cdot t$ product rule fails to predict equilibrium behaviour in aerosol neutralisers at high particle concentration and small particle size as it does not capture the influence of total particle concentration or particle size. For example, it was shown that for initially neutral 15 nm diameter particles non-equilibrium charging is found when the particle concentration is greater than one-tenth of the ion concentration. Solving the charge conservation equations for a range of ion generation rates, neutraliser residence times, particle concentrations, and particle sizes, allowed for the development of a non-dimensional approach to predict equilibrium behaviour as a function of two non-dimensional groups: $\hat{N}$ the non-dimensional ion concentration, and $\hat{\tau}$ the non-dimensional residence time. The resulting functional fit of the equilibrium indicator can be used to determine whether equilibrium has been achieved in practice. For that purpose a 3D approach is needed to correctly estimate the particle-weighted ion concentration and the particle-averaged residence time. These physically relevant values were computed using a 3D charging model in the case of TSI 3077 and 3077A neutralisers. Alternative strategies to derive these figures are suggested, and it is likely that these figures could be determined for most commercially available neutralisers. This method applies to any charging situation where the incoming aerosol is neutral, but this approach could easily be extended to the case of initially charged aerosols. Overall it is hoped this work will raise awareness of non-equilibrium issues in neutralisers. Additional progress is anticipated through additional validation of our methods and better fundamental understanding of how ion properties affect equilibrium charging in neutralisers.

## Acknowledgements

The authors express their thanks to Cambustion ltd. for the loan of the TSI 3077A neutraliser. The project was supported by the EPSRC Cambridge NanoDTC, EP/G037221/1, the Cambridge Home EU Scholarship Scheme (CHESS Fund) and the Schiff Foundation Studentships.

## Appendix A. Supporting information

Supplementary data associated with this article can be found in the online version at http://dx.doi.org/10.1016/j.jaerosci.2015.03.006.

## References

Adachi, M., Kousaka, Y., & Okuyama, K. (1984). Unipolar and bipolar diffusion charging of ultrafine aerosol particles. *Journal of Aerosol Science*, *16*(2), 109–123.
Alonso, M., & Alguacil, F.J. (2003). The effect of ion and particle losses in a diffusion charger on reaching a stationary charge distribution. *Journal of Aerosol Science*, *34*(12), 1647–1664.
Alonso, M., Kousaka, Y., Nomura, T., Hashimoto, N., & Hashimoto, T. (1997). Bipolar charging and neutralisation of nanometer-sized aerosol particles. *Journal of Aerosol Science*, *28*(8), 1479–1490.
Biskos, G., Yurteri, C.U., & Schmidt-Ott, A. (2008). Generation and sizing of particles for aerosol-based nanotechnology. *KONA Powder and Particle Journal*, *26*, 13–35.
BS ISO 15900:2009(E) (2009). *Determination of particle size distribution – differential electrical mobility analysis for aerosol particles. British Standards Institute*: .
Flagan, R.C. (2008). Differential mobility of aerosols: A tutorial. *KONA Powder and Particle Journal*, *26*, 254–268.
Fuchs, N.A. (1963). On the stationary charge distribution on aerosol particles in a bipolar ionic atmosphere. *Geofisica Pura e Applicata*, *56*(*1*), 185–193.
Gopalakrishnan, R., Meredith, M.J., Larriba-Andaluz, C., & Hogan, C.J., Jr. (2013). Brownian dynamics determination of the bipolar steady state charge distribution on spheres and non-spheres in the transition regime. *Journal of Aerosol Science*, *63*, 126–145.
Hoppel, W.A., & Frick, G.M. (1986). Ion-aerosol attachment coefficients and the steady-state charge distribution on aerosols in a bipolar ion environment. *Aerosol Science and Technology*, *5*(1), 1–21.
Hoppel, W.A., & Frick, G.M. (1990). The nonequilibrium character of the aerosol charge distributions produced by neutralizers. *Aerosol Science and Technology*, *12*(3), 471–496.
Kallinger, P., Steiner, G., & Szymanski, W. (2012). Characterization of four different bipolar charging devices for nanoparticle charge conditioning. *Journal of Nanoparticle Research*, *14*(*6*), 1–8.
Lee, H.M., Soo Kim, C., Shimada, M., & Okuyama, K. (2005). Bipolar diffusion charging for aerosol nanoparticle measurement using a soft X-ray charger. *Journal of Aerosol Science*, *36*(7), 813–839.
Levenspiel, O. (1998). *Chemical reaction engineering* 3rd ed.). John Wiley & Sons: New York.
Liu, B.Y.H., & Pui, D.Y.H. (1974). Electrical neutralization of aerosols. *Journal of Aerosol Science*, *5*(5), 465–472.
López-Yglesias, X., & Flagan, R.C. (2013). Ion–aerosol flux coefficients and the steady-state charge distribution of aerosols in a bipolar ion environment. *Aerosol Science and Technology*, *47*(6), 688–704.
Reischl, G.P., Mäkelä, J.M., Karch, R., & Necid, J. (1996). Bipolar charging of ultrafine particles in the size range below 10 nm. *Journal of Aerosol Science*, *27*(*6*), 931–949.
Steiner, G., Jokinen, T., Junninen, H., Sipilä, M., Petäjä, T., Worsnop, D., Reischl, G.P., & Kulmala, M. (2014). High-resolution mobility and mass spectrometry of negative ions produced in a $^{241}$Am aerosol charger. *Aerosol Science and Technology*, *48*(3), 261–270.
Steiner, G., & Reischl, G.P. (2012). The effect of carrier gas contaminants on the charging probability of aerosols under bipolar charging conditions. *Journal of Aerosol Science*, *54*, 21–31.
Tsoulfanidis, M. (1995). *Measurement and detection of radiation* 2nd ed.). Taylor & Francis: London.
Vasiliou, J. (2005). An evaluation of a scanning mobility particle sizer with NIST-traceable particle size standards. *NSTI-Nanotech*, *2*, 691–693.
Wiedensohler, A. (1988). An approximation of the bipolar charge distribution for particles in the submicron size range. *Journal of Aerosol Science*, *19*(*3*), 387–389.
Yun, K.M., Lee, S.Y., Iskandar, F., Okuyama, K., & Tajima, N. (2009). Effect of X-ray energy and ionization time on the charging performance and nanoparticle formation of a soft X-ray photoionization charger. *Advanced Powder Technology*, *20*(*6*), 529–536.